(untwisted boat conformation) carbon skeleton allows for the greatest simultaneous H-H and C-H bonding. Partway down the product valley, the burden shifts away from the C-H bonding and toward H-H bonding and π bonding in the ring. For a benzene fragment bent into a boat-like conformation, it may be energetically favorable to approach planarity by first twisting to obtain two 3-carbon atom groups with allylic-type resonance stabilization. If the bent benzene fragment wanted to twist to enhance resonance stabilization, then the leaving H_2 would experience a torque that would excite rotation in the plane of the carbon skeleton.

Acknowledgments. This research was supported by the Office of Naval Research through the Naval Research Laboratory and by the National Science Foundation. R.J.R. acknowledges support through the Office of Naval Research Graduate Fellowship Program.

Registry No. 1,4-Cyclohexadiene, 628-41-1.

Relative Basicities of the Oxygen Sites in $[V_{10}O_{28}]^{6-}$. An Analysis of the ab Initio Determined Distributions of the Electrostatic Potential and of the Laplacian of Charge Density

Jean-Yves Kempf,[†] Marie-Madeleine Rohmer,[§] Josep-Maria Poblet,[‡] Carles Bo,[‡] and Marc Bénard*[,§]

Contribution from the Laboratoire de Chimie Quantique, U.P.R. 139 du CNRS, Université Louis Pasteur, F-67000 Strasbourg, France, the Departament de Quimica, Universitat de Barcelona, 43005 Tarragona, Spain, and the Laboratoire de Résonance Magnétique Nucléaire et Modélisation Moléculaire (RM3), U.R.A. 422 du CNRS, Université Louis Pasteur, F-67000 Strasbourg, France. *Received June 27, 1991*

Abstract: An ab initio SCF wave function has been generated for the ground state of the $[V_{10}V_{28}]^{6-}$ ion, with a basis set of triple-zeta quality for the valence shell of oxygen. This wave function has been the starting point for theoretical studies on the relative basicities of the six external oxygen sites of the title ion in order to interpret the experimental findings concerning the preferred sites of proton fixation. The topology of the distribution of electrostatic potentials (ESP) around the ion is deduced from the determination of $V(r)$ in some specific planes and on spherical surfaces centered on each of the six oxygen sites. Several ESP minima not equivalent by symmetry have been characterized, most of them, but not all, lying in the vicinity of a specific oxygen atom. The two deepest nonequivalent ESP minima are associated with the two distinct sites, referred to as O_B and O_C, undergoing protonation in $[H_3V_{10}O_{28}]^{3-}$. An analysis of the Laplacian of the charge density shows that the direction of the maxima in $-\nabla^2\rho$ which characterize local charge concentrations around the oxygen atoms, coincides within a few degrees with the direction of the ESP minima when existing, and with that of the protons in $[H_3V_{10}O_{28}]^{3-}$ in the vicinity of sites O_B and O_C.

1. Introduction

The problem we are interested in the present article originated in an experimental investigation by Day and co-workers on the title ion.[1] These authors noticed that the closest packed surface of the $[V_{10}O_{28}]^{6-}$ ion consists of a highly congested nine-atom array centered around oxygen site B (Figures 1 and 2). This surface is particularly appealing to study the conditions that decide the fixation mode of inorganic, organometallic, or organic groups to one or several oxygen atoms. In order to delineate the factors, including steric congestion, that influence those incorporation processes,[2] it was necessary to decide first what oxygen on the surface is basic enough to serve as a bonding site for small cationic groups. The crystal structure of $[H_3V_{10}O_{28}]^{3-}$ (**1**) was then determined by Day et al. with sufficient accuracy to locate the protons.[1] In the same work, the position of the protons was also assigned in $[H_2V_{10}O_{28}]^{4-}$ (**2**, crystal), and the predominant protonation site was determined in $[HV_{10}O_{28}]^{5-}$ (**3**, aqueous solution). Eventually, this study proved to be inconclusive in determining unambiguously the most basic oxygen site on the surface of $[V_{10}O_{28}]^{6-}$. The protonation sites in $[H_3V_{10}O_{28}]^{3-}$ (two C sites surrounding one B oxygen and leading to hydrogen-bound dimers (Figure 3)) and those in $[H_2V_{10}O_{28}]^{4-}$ (two oxygen C sites opposite with respect to the center of symmetry) are not consistent with going from **1** to **2**, through a single deprotonation. A similar change in the protonation sites occurs between **2** and **3**, suggesting that protonation induces a nonlocal charge reorganization modifying the scale of basicities of the unperturbed $[V_{10}O_{28}]^{6-}$ ion.[1] However, a former determination of protonation sites in $[V_{10}O_{28}]^{6-}$ by ^{17}O nuclear magnetic resonance led to the conclusion that O_B is the predominant protonation site whereas O_C is protonated to a lesser extent.[3] The goal of the present work is a quantitative determination of this scale of basicities on the six external sites of $[V_{10}O_{28}]^{6-}$ through an investigation of the three-dimensional distribution of the electrostatic potential (ESP), defined in every point of space as

$$V(r) = \sum_A \frac{Z_A}{|r - R_A|} - \int \frac{\rho(r')}{|r - r'|}\,dr' \qquad (1)$$

where Z_A represents the nuclear charge of atom A, and $\rho(r')$ corresponds to the molecular electron density functional, determined from an ab initio SCF wave function. The gradient and Laplacian distributions of the computed electron density have also been derived and analyzed in connection with the ESP minima and with the X-ray determined orientation of the protons in $[H_3V_{10}O_{28}]^{3-}$.

[†] Laboratoire RM3, Université Louis Pasteur.
[§] Laboratoire de Chimie Quantique.
[‡] Universitat de Barcelona.

(1) Day, V. W.; Klemperer, W. G.; Maltbie, D. J. *J. Am. Chem. Soc.* **1987**, *109*, 2991.
(2) (a) Besecker, C. J.; Day, V. W.; Klemperer, W. G.; Thompson, M. R. *J. Am. Chem. Soc.* **1984**, *106*, 4125. (b) Day, V. W.; Klemperer, W. G.; Schwartz, C. *Ibid.* **1987**, *109*, 6030.
(3) Klemperer, W. G.; Shum, W. *J. Am. Chem. Soc.* **1977**, *99*, 3544.

0002-7863/92/1514-1136$03.00/0

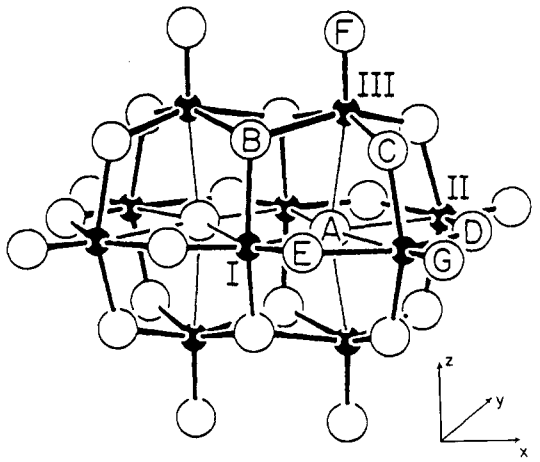

Figure 1. Schakal drawing of the $[V_{10}O_{28}]^{6-}$ ion (reproduced from ref 1 with permission).

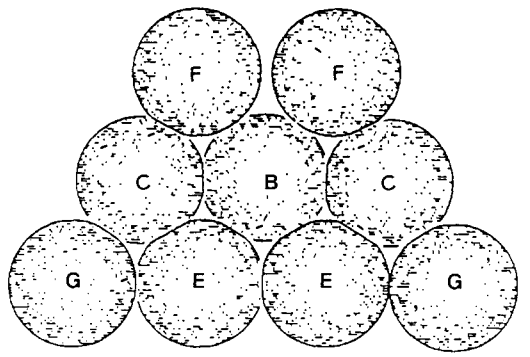

Figure 2. The closest packed oxygen surface of the $[V_{10}O_{28}]^{6-}$ ion (adapted from ref 1 with permission).

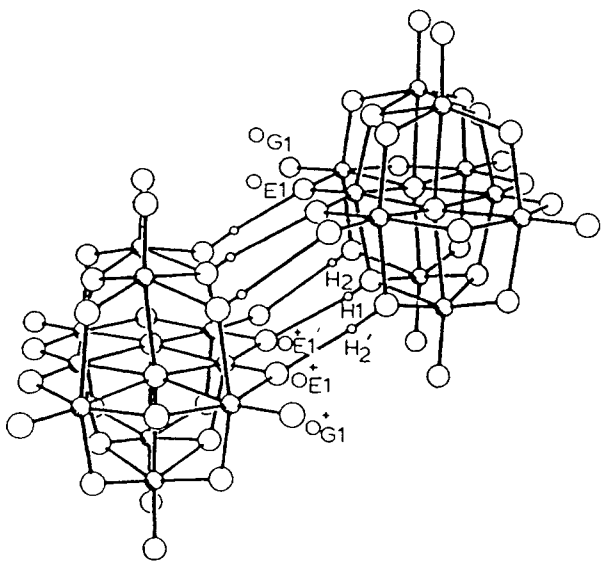

Figure 3. Perspective ORTEP plot of the $[H_3V_{10}O_{28}]_2^{6-}$ dimer found in crystalline $H_3V_{10}O_{28}[(C_6H_5)_4P]_3 \cdot 4CH_3CN$ (reproduced from ref 1 with permission).

2. Computational Details

The geometry used for the SCF calculation of $[V_{10}O_{28}]^{6-}$ has been taken from the averaging proposed by Day et al.[1] of the structure of $Na_6V_{10}O_{28} \cdot 18H_2O$.[4] The symmetry point group of the averaged ion is D_{2h}, defining the three types of vanadium atoms and the seven distinct oxygen sites represented in Figure 1. An all-electron SCF calculation

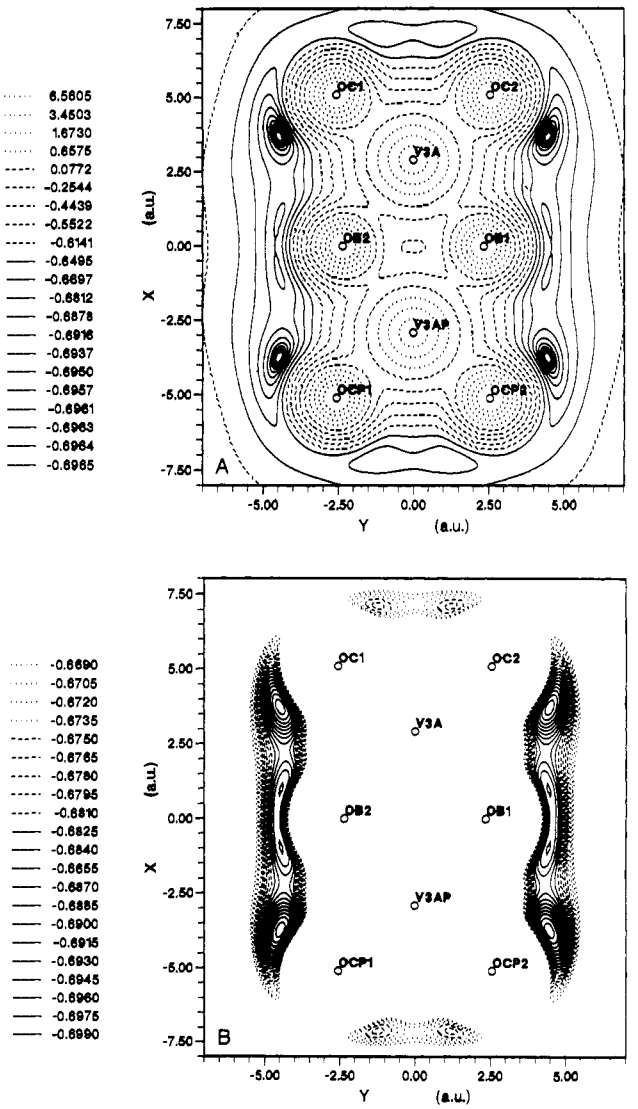

Figure 4. Section of the electrostatic potential for $[V_{10}O_{28}]^{6-}$: plane containing two O_B and four O_C oxygen sites. (A, top) Lowest contour, −0.6965 hartree; first contour interval, 7.5×10^{-5} hartree; successive contour intervals increased by a factor 1.75. (B, bottom) All contour intervals equal to 0.0015 hartree.

has then been carried out on the Cray-2 computer of the Ecole Polytechnique de Lausanne (EPFL, Switzerland), using the Cray version of the ASTERIX program system.[5,6] The basis set used for vanadium was the (11,7,5) set of Hyla-Krypsin et al.,[7] contracted into [3,2,2], that is minimal for the inner shells and double-ζ for the valence d shell. In view of the largely ionic nature of the metal oxide, the highly positive V(V) atoms were stripped from their outer sp shell, and no diffuse function has been added to the standard 3d valence shell, in return for which it became technically possible to provide a better description for the negatively charged oxygen atoms. A basis set of triple-ζ quality for the valence shell was selected for oxygen by adding one s function (exp 0.09) and one p function (exp 0.07) to the (9,5) set of Huzinaga.[8] The basis set for oxygen is therefore (10,6) contracted into [4,3]. More technical details

(4) (a) Pullman, N. Ph.D. Dissertation, Rutgers University, 1966; *Diss. Abstr.* **1967**, *28B*, 140. (b) Durif, A.; Averbuch-Pouchot, M. T.; Guitel, J. C. *Acta Crystallogr.* **1980**, *B36*, 680.

(5) (a) Ernenwein, R.; Rohmer, M.-M.; Bénard, M. *Comp. Phys. Commun.* **1990**, *58*, 305. (b) Rohmer, M.-M.; Demuynck, J.; Bénard, M.; Wiest, R.; Bachmann, C.; Henriet, C.; Ernenwein, R. *Ibid.* **1990**, *60*, 127. (c) Wiest, R.; Demuynck, J.; Bénard, M.; Rohmer, M.-M.; Ernenwein, R. *Ibid.* **1991**, *62*, 107.

(6) Rohmer, M.-M.; Ernenwein, R.; Ulmschneider, M.; Wiest, R.; Bénard, M. *Int. J. Quantum Chem.* **1991**, *40*, 723.

(7) Hyla-Krypsin, I.; Demuynck, J.; Strich, A.; Bénard, M. *J. Chem. Phys.* **1981**, *75*, 3954.

(8) Huzinaga, S. Technical Report; University of Alberta: Edmonton, Canada, 1971.

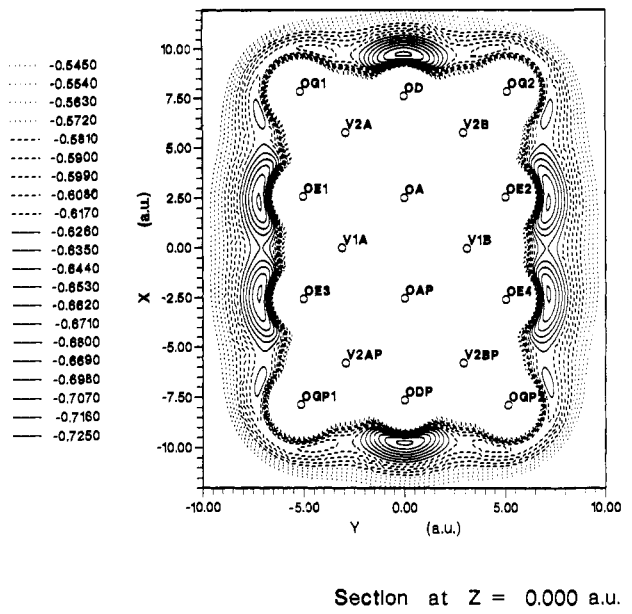

Figure 5. Section of the electrostatic potential for $[V_{10}O_{28}]^{6-}$: xy plane containing the A, D, E, and G sites. All contour intervals equal to 0.009 hartree.

about this calculations are given in ref 6.

Electrostatic potentials have been computed (i) for planar grids of points defined in planes containing several oxygen sites and (ii) for spherical grids centered on an oxygen site and represented in two dimensions by means of a stereographic projection.[9] Both the planar and the projected spherical maps have been represented using the PANORAMIX graphical package.[10] Finally, the topological properties of the charge density and its derivatives have been computed using a modified version of the AIMPAC package of programs,[11] kindly provided by R. F. W. Bader.

3. Topology of the Electrostatic Potential (ESP) Distribution

In a preliminary investigation,[6] the electrostatic potential distribution had been displayed in two parallel planes respectively containing (i) the B and C oxygen sites (Figure 4) and (ii) the A, D, E, and G sites (Figure 5). For those planes and throughout the present study, two complementary methods of representation have been used. In Figure 4a, successive contour intervals are increased by a factor 1.75 starting from a value close to that of the deepest minimum, −0.6969 hartree, and from a first interval of 7.5×10^{-5} hartree. In Figure 4B, the distribution of the electrostatic potential in the same plane is represented with all contour intervals taken equal to 1.5×10^{-3} hartree. Constant, but larger contour intervals (9×10^{-3} hartree) have been selected for the plane representation in Figure 5.

The two deepest minima *in the considered planes* both appear in the section containing the B and C sites (Figure 4). One is a narrow gorge with a double minimum at −0.689 hartree separated by a shallow saddle point at −0.688 hartree. The other deepest potential well and its symmetry-related equivalents (−0.6969 hartree) are clearly connected to the C sites. In the same plane, a third minimum, higher in energy (−0.680 hartree), is also connected to the C sites (Figure 4). This first insight into the distribution of the electrostatic potential agrees with the experimental evidence that oxygen atoms B and C are altogether the preferred sites for proton fixation.[1] As a matter of fact, the map of Figure 5 containing the other oxygen sites displays a series of minima all significantly higher in energy than those respectively connected to O_B and O_C. The lowest minima in that plane are respectively facing sites D (−0.681 hartree) and E (−0.671 hartree).

The information contained in those sections is obviously not sufficient to conclude about the relative basicity of the oxygen sites. There is no reason for the real ESP minima to lie in a "horizontal" plane (z = 3.47 bohrs) containing most oxygen and vanadium atoms. Figure 6, which displays the ESP in the yz half-plane containing two V_1 and two O_B sites (all contour intervals equal to 5×10^{-3} hartree), confirms this statement. The minimum obtained in this plane (−0.720 hartree) is shifted out of the horizontal plane by 33° with respect to the O_B nucleus. However, it appears from the planar maps of Figures 4–6 that the relative minima reported in the considered planes seem to be connected each to a specific oxygen site and located in a narrow range of distances comprised between 2.1 and 2.4 bohrs from the considered atoms. This suggests a strategy for refining at a relatively low cost our knowledge of the topology of the ESP distribution. Rather than considering planes, spherical sections centered on a given oxygen atom should allow for the location of the real minima by just varying the radius of the sphere between 2.1 and 2.4 bohrs. This strategy was quite successful for sites B, C, D, and G. The stereographic projections of the spherical sections containing the minima (or very close to it) are displayed in Figures 7–10. The left-hand-side circle represents the projection of the "upper" hemisphere, that is, the collection of points with $|z| \geq |z_{center}|$, referring to the axis system of Figure 1. The respective values of the minima are −0.7201 hartree for B, at r = 2.140 bohrs; −0.7040 hartree for C (r = 2.196 bohrs); −0.6829 hartree for D (2.195 bohrs); and −0.6315 hartree for G (2.335 bohrs). Around B and C sites, the minimum is unique. For B (Figure 7), it is contained in the plane of symmetry defined by the four B sites and therefore shows up in the planar section of Figure 6. Note that the minimum is located in the projection of the upper hemisphere, which is consistent with z_{min} being larger than z_{O_B} in Figure 6. The circumference of the stereographic projection corresponds to the section of the sphere with the horizontal plane of Figure 4, and the narrow valley of potential noticed in the plane is clearly recognizable around the "south pole" of the projection.

A unique minimum, located too in the upper sphere, is also characterized around the C sites (Figure 8). This real, though secondary minimum is less stable by 10 kcal mol^{-1} than the one associated with the B sites, even though the opposite trend had been obtained from the planar section of Figure 4. The behavior of the electrostatic potential function along the circumference also explains why an artificial secondary minimum had been obtained around O_C in the planar section of Figure 4.

Potential minima connected to an oxygen atom have also been characterized around D and G sites. At variance from the situation around O_B and O_C, the minima around O_D and O_G are twin, located on either side of the xy symmetry plane containing the oxygen atoms. The two minima are separated by a shallow saddle point in the xy plane, so that they generate half-circular valleys extending around the considered oxygen site. Such valleys around the D sites appear in the section of the xz plane represented in Figure 11. The twin minima associated with D are higher by 23 and by 13 kcal mol^{-1} respectively than the potential wells connected with O_B and O_C. The minima associated with O_G, the most external atom of the closest packed surface of Figure 2, is still higher than those of O_D by more than 30 kcal mol^{-1} (Figure 5).

No potential minimum could be detected around oxygen sites E and F by just varying the radius of the sphere between 2.1 and 2.5 bohrs. Around F, the ESP is steadily decreasing when expanding the sphere, and the lowest value remains in the xz symmetry plane containing the four F sites, so that this planar section was eventually generated (Figure 11). A minimum is found along the z axis separating the closest F sites, at 3.0 bohrs from those O_F atoms, and 5.1 bohrs from the two closest O_B atoms. In the present case, the obtained minimum (−0.6818 hartree) cannot be associated with any specific oxygen atom, but with the basin composed of the four neighboring F and B atoms mentioned above (see Figure 1).

The case of the E sites, for which no minimum could be characterized from an exploration of the spherical surfaces, appears somewhat different. Figure 12 displays the ESP in the plane parallel to yz and containing two E and two F sites. Four minima

(9) Stevens, E. D.; Coppens, P. *J. Cryst. Mol. Struct.* **1978**, 251.
(10) Wiest, R.; Spĕri, M. PANORAMIX, graphical facilities for ASTERIX, unpublished.
(11) Biegler-Konig, F. W.; Bader, R. F. W.; Tang, T. H. *J. Comput. Chem.* **1982**, *3*, 317.

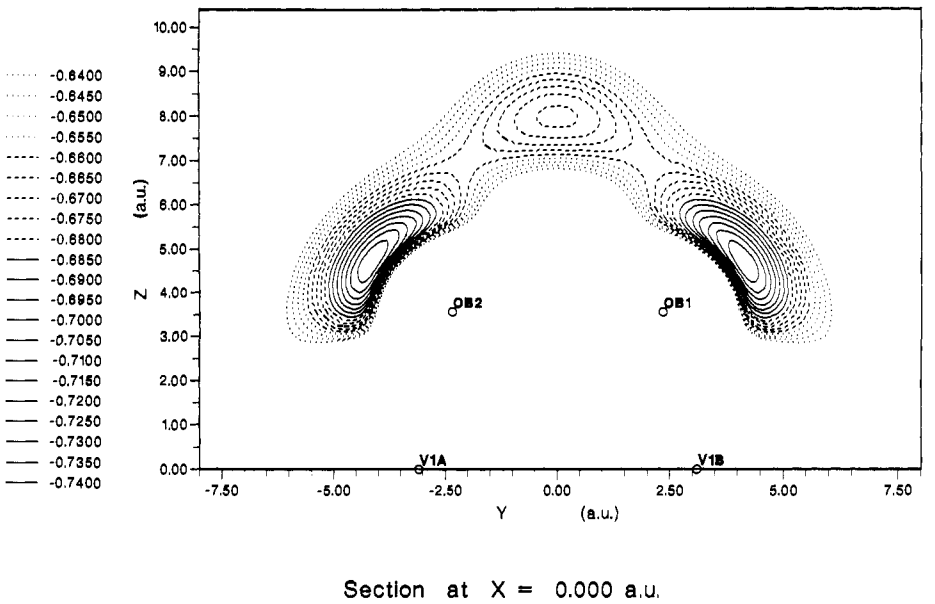

Figure 6. Section of the electrostatic potential for $[V_{10}O_{28}]^{6-}$: *yz* half-plane containing two V_1 and two O_B sites. All contour intervals equal to 0.005 hartree.

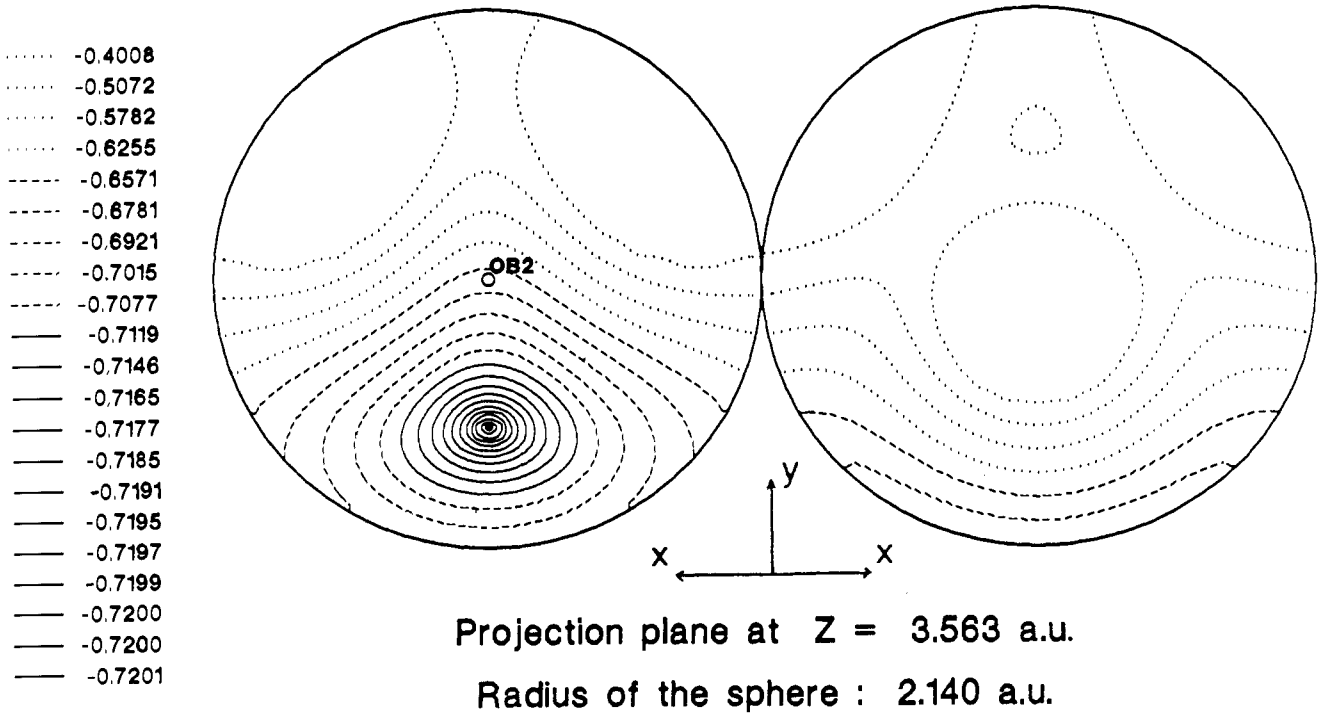

Figure 7. $[V_{10}O_{28}]^{6-}$: stereographic projection of the ESP computed on a sphere of radius 2.14 bohrs, centered on O_{B_2} (see Figure 4). Lowest contour, −0.720090 hartree; first contour interval, 4.8×10^{-5} hartree; successive contour intervals increased by a factor 1.5.

do show up in this plane, located each at 4.0 bohrs from an E site and 5.3 bohrs from a F site, and corresponding to a *z* value of ±3.8 bohrs. Figure 5 reports the potential distribution in a plane perpendicular to the latter one at a *z* value close to that of the minima (*z* = 3.47 bohrs). The comparison of those two maps shows that the minima of Figure 12 are, in fact, saddle points connecting the deep wells respectively associated with neighboring B and C sites. Now going back to the relative minima (−0.671 hartree) facing each E site in Figure 4, it becomes obvious from Figure 12 that they are saddle points at the top of opposite valleys that bifurcate later on (Figure 5) toward the real minima characterized around B (Figure 7) and C (Figure 8).

To summarize, deep wells of electrostatic potential, at −0.7201 and −0.7040 hartree, can be associated with oxygen sites B and C, respectively. Those minima, characterized from the exploration of spherical surfaces, show up in the upper hemisphere with respect to the *z* coordinate of the oxygen center. This is in agreement with the orientation of the protons attached to neighboring C, B, and C sites in $[H_3V_{10}O_{28}]^{3-}$ (Figure 3).[1] A more detailed comparison between the respective orientation of the protons in **1**, of the ESP minima, and of the critical points of charge concentration (see next section) is displayed in Table II. Other ESP minima have been characterized around D sites (−0.6829 hartree), G sites (−0.6315 hartree), and in the basin defined by four neighboring O_F and O_B atoms (−0.6818 hartree). No ESP minimum could be characterized in the vicinity of E sites.

4. Distribution of the Computed Charge Density: Gradient and Laplacian of ρ_{mol}

The electrostatic potential at a given point represents the sum of attractions and repulsions respectively due to the nuclear point charges and to the distribution of the molecular electron density

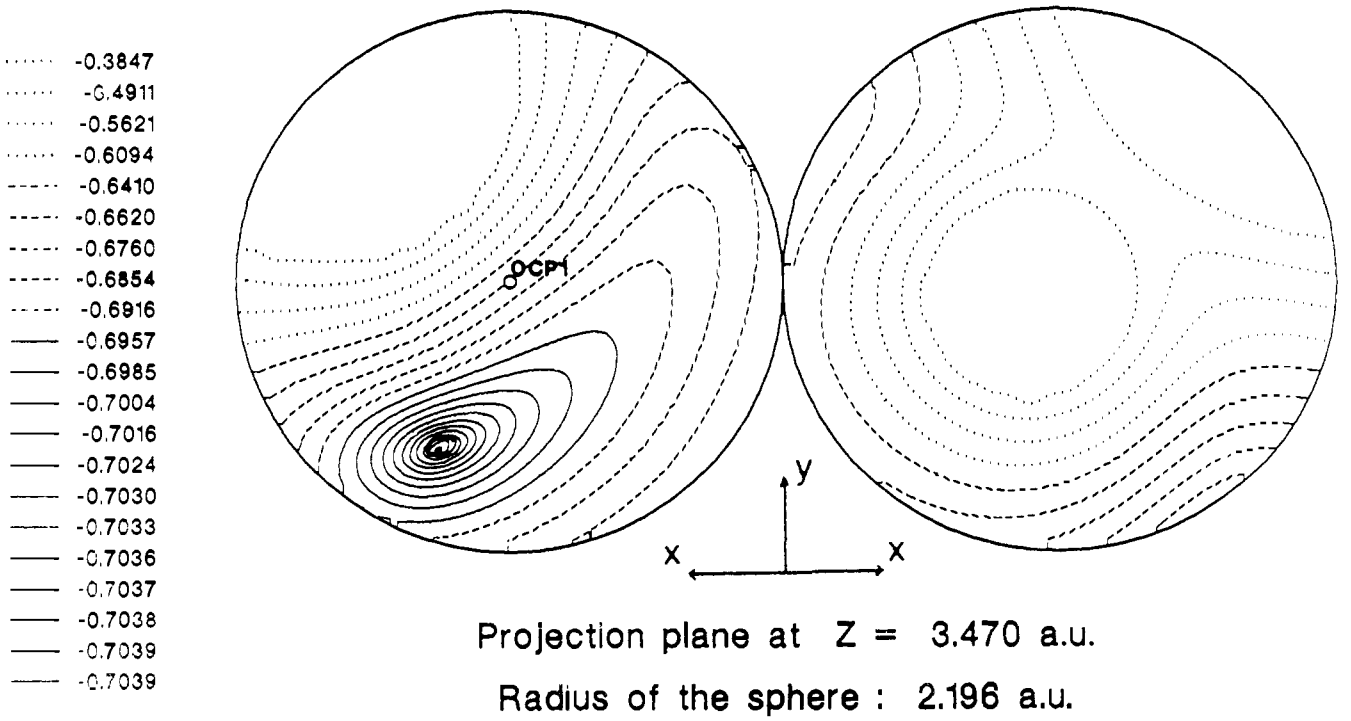

Figure 8. $[V_{10}O_{28}]^{6-}$: stereographic projection of the ESP computed on a sphere of radius 2.196 bohrs, centered on O_{CP_1} (see Figure 4). Lowest contour, −0.703950 hartree; contour intervals as in Figure 7.

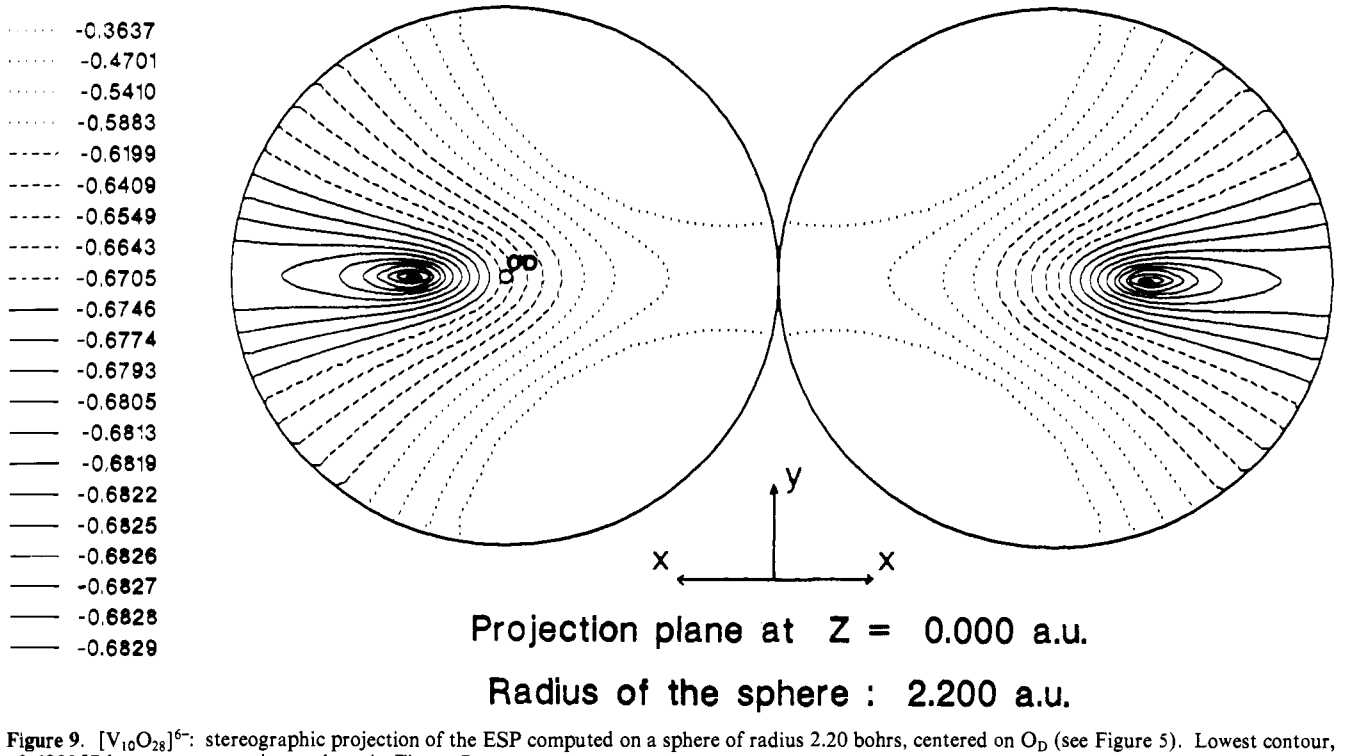

Figure 9. $[V_{10}O_{28}]^{6-}$: stereographic projection of the ESP computed on a sphere of radius 2.20 bohrs, centered on O_D (see Figure 5). Lowest contour, −0.682857 hartree; contour intervals as in Figure 7.

extending over the whole space, as indicated in (1). Because of the long-range character of the electrostatic force, it is intuitively expected that the ESP minima should reflect in some way the steric congestion of the oxygen sites having a large number of negatively charged nearest neighbors, all contributing to decrease the ESP. Indeed, the lowest ESP minimum is characterized in the vicinity of site B, which is located at the center of the planar closest packed oxygen surface (Figure 2). Then, the next lowest minimum is connected to the C sites, also located in the central layer of this surface (Figure 2). On the opposite way, the ESP secondary minimum highest in energy has been characterized in the vicinity of the G sites, which are the most external atoms of the same surface. The relative ordering of the ESP minima characterized around $[V_{10}O_{28}]^{6-}$ then appears clearly related to the degree of steric congestion specific to the neighboring atom. However, local factors also happen to play a large role in the topology of the ESP distribution, since they determine the existence of minima around most oxygen sites, even the less crowded ones, and they influence the orientation of these potential wells, including the deepest ones. The next part of the present study is devoted to the analysis of those local factors.

Bader et al.[12-14] have proposed a new definition of the interaction

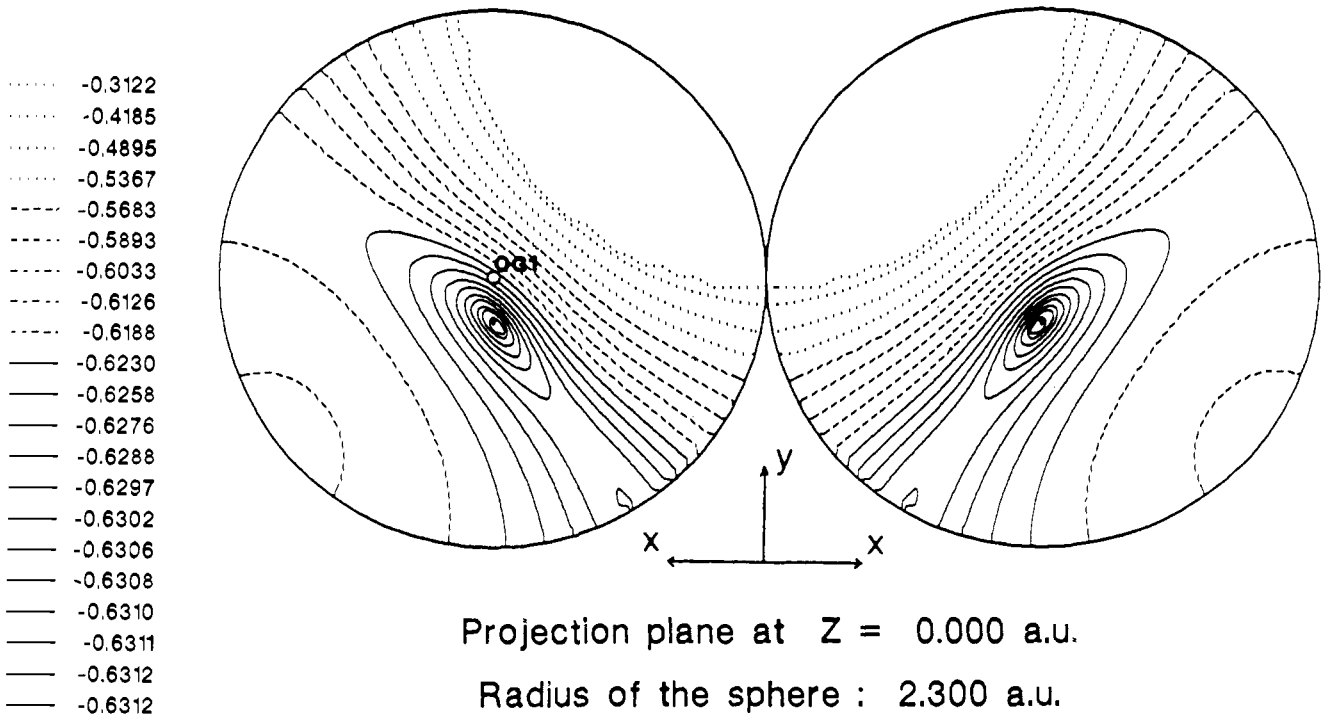

Figure 10. $[V_{10}O_{28}]^{6-}$: stereographic projection of the ESP computed on a sphere of radius 2.30 bohrs, centered on O_{G_1} (see Figure 5). Lowest contour, −0.631202 hartree; contour intervals as in Figure 7.

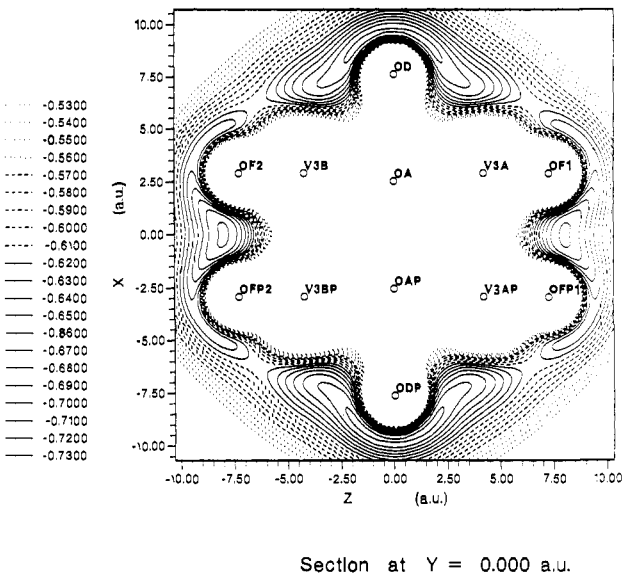

Figure 11. Section of the electrostatic potential for $[V_{10}O_{28}]^{6-}$: *xz* plane containing the A, D, and F sites. All contour intervals equal to 0.010 hartree.

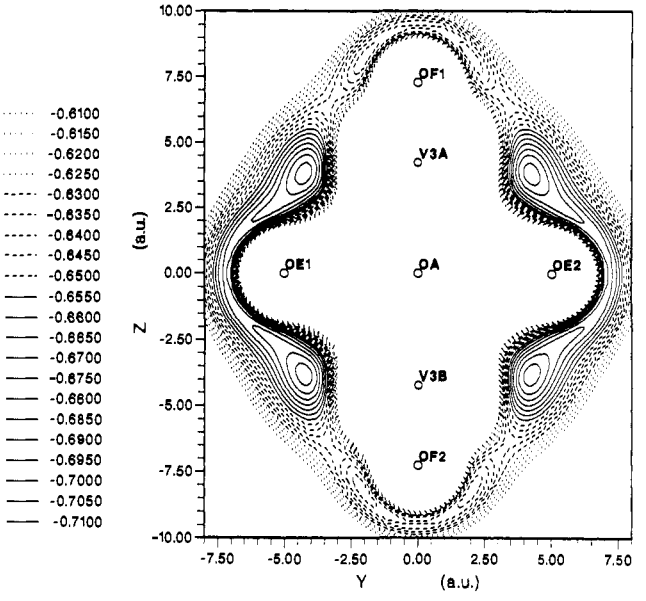

Figure 12. Section of the electrostatic potential for $[V_{10}O_{28}]^{6-}$: plane parallel to *yz* and containing two E sites. All contour intervals equal to 0.005 hartree.

of atoms in molecules based upon the topology of the molecular charge density ρ, deduced from the critical points of its associated fields.[15,16] A connection has been established between the structure of a molecular system and the gradient vector field ∇, introducing the concept of bond path. A bond path is defined as a ridge of density connecting two nuclei. According to Bader et al., the presence of a bond path at the equilibrium geometry represents a necessary and sufficient condition to the existence of a bond.[12-16] Such bond paths and the associated (3, −1) bond critical points (cp) corresponding to $\nabla\rho = 0$ could be characterized in the computed density distribution of $[V_{10}O_{28}]^{6-}$ between all neighboring V–O pairs. The values of $\nabla^2\rho$ (au) and bond ellipticities $\epsilon = (\lambda_1/\lambda_2) - 1$ (λ_1 and λ_2, with $|\lambda_1| < |\lambda_2|$ representing the two negative curvatures of ρ of the bond cp) are collected in Table I for all V–O bonds. A very accurate inverse correlation is found between $\rho(r_c)$ and the corresponding V–O bond length (Table I). Such a linear relationship between the bond distance and the density at the critical point $\rho(r_c)$ had been previously noticed by Bader et al. for C–C bonds with various bond orders in ethane, benzene, ethylene, and acetylene.[15] These authors had taken advantage of this correlation to propose a relationship between the value of $\rho(r_c)$ and the C–C bond order. The situation

(12) Bader, R. F. W.; Essēn, H. *J. Chem. Phys.* **1984**, *80*, 1943.
(13) Bader, R. F. W., MacDougall, P. J.; Lau, C. D. H. *J. Am. Chem. Soc.* **1984**, *106*, 1594.
(14) Bader, R. F. W. *Acc. Chem. Res.* **1985**, *18*, 9.
(15) Bader, R. F. W.; Slee, T. S.; Cremer, D.; Kraka, E. *J. Am. Chem. Soc.* **1983**, *105*, 5061.
(16) Low, A. A.; Kunze, K. L.; MacDougall, P. J.; Hall, M. B. *Inorg. Chem.* **1991**, *30*, 1079.

Table I. V–O Bond Properties in the $[V_{10}O_{28}]^{6-}$ Ion

bond	d_{V-O} (Å)	$\rho(r_c)$(au)[a]	$\nabla^2\rho(r_c)$(au)[b]	ϵ[c]
V_2-O_G	1.605	0.249	0.926	0.002
V_3-O_F	1.614	0.246	0.933	0.014
V_1-O_E	1.697	0.200	0.723	0.045
V_3-O_C	1.826	0.144	0.515	0.013
V_2-O_D	1.831	0.141	0.506	0.027
V_2-O_C	1.883	0.125	0.441	0.045
V_1-O_B	1.927	0.114	0.398	0.036
V_3-O_B	2.013	0.092	0.357	0.071
V_2-O_E	2.032	0.082	0.351	0.072
V_1-O_A	2.116	0.070	0.315	0.007
V_3-O_A	2.243	0.050	0.268	0.015
V_2-O_A	2.316	0.041	0.229	0.038

[a] 1 au = 6.748 e Å^{-3}. [b] 1 au = 24.10 e Å^{-5}. [c] Bond ellipticity.

is somewhat different in the present case. None of the V–O bond ellipticities is significantly different from zero (Table I). No π or oxo character can therefore be detected from this analysis, even for the very short $V_2 - O_G$ (1.605 Å) or $V_3 - O_F$ (1.614 Å) bonds connecting a vanadium atom to a terminal oxygen. The $\rho(r_c)$ values range from 0.050 au (0.277 eÅ^{-3}) for the longest V–O bond ($V_2 - O_A$, 2.316 Å) to the relatively high value of 0.249 au (1.680 eÅ^{-3}) for $V_2 - O_G$. All the V–O bonds are characterized by a very large positive curvature at the bond critical point along the direction of the bond path (λ_3). The value of $\nabla^2\rho(r_c)$, which equals the sum of the three curvatures of the density at the critical point, is largely dominated by λ_3 and therefore positive for the whole range of the V–O distances. It has been shown that positive values of $\nabla^2\rho$ in the interatomic surface are characteristic of "closed-shell interactions" governed by the contraction of the charge density toward each of the interacting nuclei.[13,17,18] Ionic bonds are a typical case of such interactions,[19] and recent studies on the coordinative bond indicate that the metal–ligand interaction with pure σ-donor or σ-donor and π-acceptor ligands also yield positive values of $\nabla^2\rho(r_c)$.[16,20,21] The regions of charge depletion are represented by solid lines in Figure 13 displaying three maps of $\nabla^2\rho$ in the *xy*, *xz*, and *yz* planes of $[V_{10}O_{28}]^{6-}$, respectively. Only three shells of charge concentration are characterized around each vanadium atom, the third shell being referred to as the inner-valence shell of charge concentration or i-VSCC.[22] The outer-valence shell of charge concentration (o-VSCC), corresponding to the $(n + 1)$s/p metal electrons seems to be often lacking in transition metals. Recent analyses of $\nabla^2\rho$ in metal atoms[23] and transition metal complexes[21,22] have failed to detect the o-VSCC, except around manganese in $Mn_2(CO)_{10}$.[24] The elusive character of the o-VSCC has been attributed to the low population and to the diffuse character of the $(n + 1)$s and $(n + 1)$p orbitals.[22]

The maps of Figure 13 show that the distribution of $\nabla^2\rho$ around oxygen atoms exhibits a very low polarization. The Laplacian distribution remains close to the spherical symmetry for all oxygen sites, suggesting for those atoms a certain closed-shell character consistent with their high negative charge. In agreement with the pattern of the Laplacian distribution in ionic bonds,[17-19] small charge concentrations appear for some oxygen atoms *in the nonbonding regions*. Let us consider, for instance, the case of a D-type oxygen in bridging position between two V_2 atoms. The Laplacian distribution does not exhibit any (3, −3) critical point (local maximum) in the *xy* bonding plane (Figure 13A). Two symmetric charge concentrations appear, however, in the non-

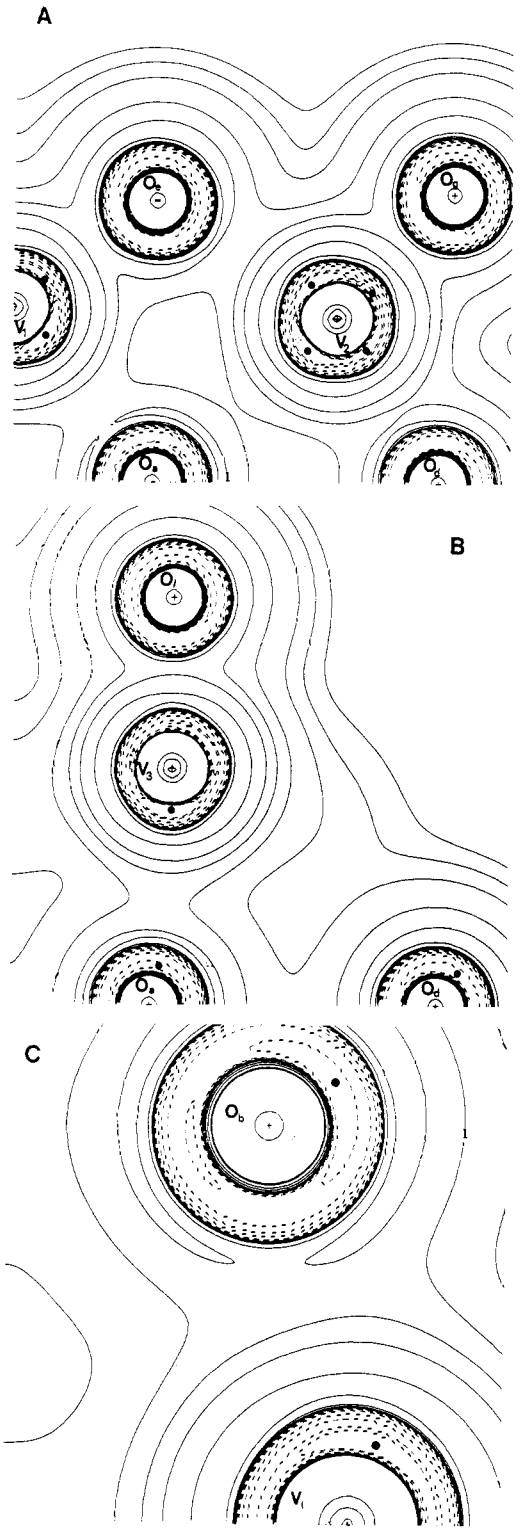

Figure 13. Plot of $\nabla^2\rho$ in three perpendicular planes containing the center of symmetry of $[V_{10}O_{28}]^{6-}$: (A) *xy* plane, (B) *xz* plane, (C) *yz* plane. Solid lines for $\nabla^2\rho > 0$ (regions of charge depletion); dotted lines for $\nabla^2\rho < 0$ (regions of charge concentration). Large dots represent the (3, −3) critical points of charge concentration.

bonding region (plane *xz*, Figure 13B) corresponding to a value of −2.84 au for $\nabla^2\rho$. The location of the critical points and the corresponding values of $\nabla^2\rho$(au) are displayed in Figure 14, and reported in Table II. All oxygen sites, except for O_B, exhibit twin charge concentrations in the nonbonding area. Since oxygen B is connected to three vanadium atoms, the only remaining nonbonding direction is the one opposite to the metallic tripod. As a matter of fact, a unique region of charge concentration is detected around this site, in the expected direction. The directions

(17) Bader, R. F. W.; Preston, H. J. T. *Int. J. Quantum Chem.* **1969**, *3*, 327.
(18) MacDougall, P. J.; Schrobilgen, G. J.; Bader, R. F. W. *Inorg. Chem.* **1989**, *28*, 763.
(19) Bader, R. F. W.; Henneker, W. *J. Am. Chem. Soc.* **1965**, *87*, 3063.
(20) Lin, Z.; Hall, M. B. *Inorg. Chem.* **1991**, *30*, 646.
(21) Bo, C.; Poblet, J. M.; Bénard, M. *Chem. Phys. Lett.* **1990**, *169*, 89.
(22) MacDougall, P. J.; Hall, M. B.; Bader, R. F. W.; Cheeseman, J. R. *Can. J. Chem.* **1989**, *67*, 1842.
(23) (a) Shi, Z.; Boyd, R. J. *J. Chem. Phys.* **1988**, *88*, 4375. (b) Sagar, R. P.; Ku, A. C. T.; Smith, V. H., Jr. *Ibid.* **1988**, *88*, 4367.
(24) MacDougall, P. J. The Laplacian of the electronic charge distribution. Ph.D. Thesis, McMaster University, Hamilton, Ont., Canada, 1989.

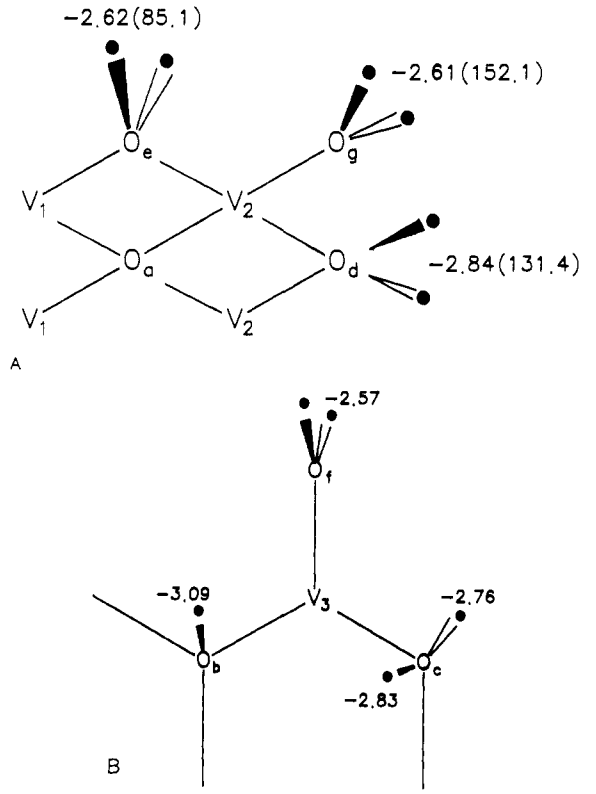

Figure 14. Characterization of the (3, −3) critical points of the Laplacian of ρ in the vicinity of the external oxygen sites: (A) D, E, and G sites; (B) B, C, and F sites. The values of $\nabla^2\rho$ and (in parentheses) the cp–O–cp′ angles are provided.

Table II. Angular Direction of the Maxima in $-\nabla^2\rho$, of the ESP Minima, and of the Protons in $[H_3V_{10}O_{28}]^{3-}$ (deg), Defined with Respect to the Next Oxygen Site and to the neighboring Atoms

angle	X = $-\nabla^2\rho(r_{cp})$	X = ESP_{min}	X = H	$-\nabla^2\rho(r_{cp})$ (au)	ESP_{min} (hartree)
XO_BV_3	117.9	115.0	107.9[a]		
			129.5[a]	3.09	−0.7201
XO_BV_1	105.8	111.2	112.4[a]		
XO_CV_3	107.3	112.5	117.3		
XO_CV_2	105.2	109.9	113.8	2.83	−0.7040
$XO_CV_3O_F$[b]	68.5	60.8	46.5		
XO_CO_B	65.7	71.6	81.8		
XO_CX'	125.2				
$X'O_CV_3$	102.2				
$X'O_CV_2$	103.1			2.76	
$X'O_CV_3O_F$[b]	64.5				
$X'O_CO_B$	147.4				
XO_DV_2	102.5	108.6		2.84	−0.6829
XO_DX'	131.4	106.3			
XO_EV_2	125.6				
XO_EV_1	101.0			2.63	
XO_EX'	85.1				
XO_GV_2	103.5	103.7			
XO_GX'	152.1	142.2		2.61	−0.6315
$XO_GV_2O_D$[b]	93.2	103.2			
XO_FV_3	110.5				
XO_FX'	133.1			2.57	(−0.6818)[c]
$XO_FV_3O_C$[b]	52.3				
XO_AV_3	3.9			2.41	
XO_AX'	162.0				

[a] The proton is not located in the *xz* plane. [b] Dihedral angle. [c] ESP minimum not directly associated with site F (see text).

of the maxima of $-\nabla^2\rho$ are defined in Table II with respect to the neighboring atoms. This table shows that the direction of each ESP minimum differs by no more than a few degrees from that

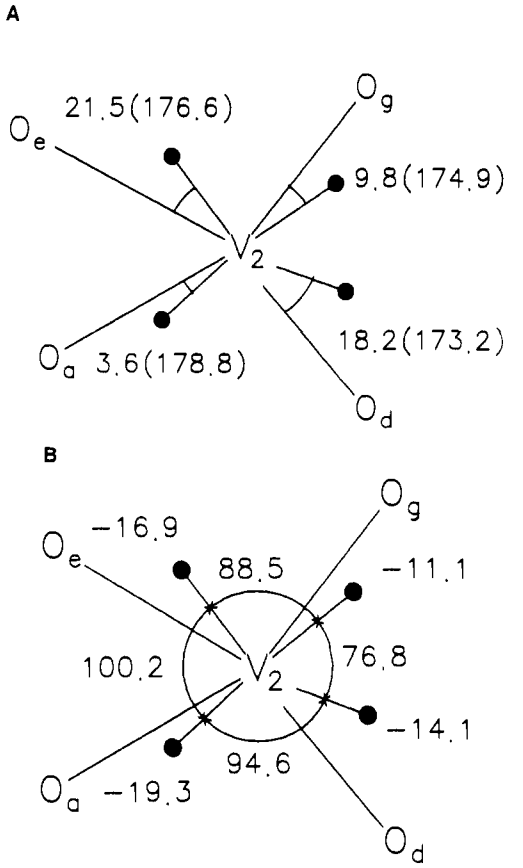

Figure 15. Characterization of the (3, −3) cp of $\nabla^2\rho$ (large dots) in the vicinity of the V_2 atoms. (A) Angular deviation of the V_2–cp direction with respect to the next V–O bond, and (in parentheses) with respect to the opposite V–O bond. (B) Values of $\nabla^2\rho$ and cp–V–cp′ angles.

of a charge concentration. Moreover, Table II also shows that the protons attached to sites B and C in $[H_3V_{10}O_{28}]^{3-}$ have been trapped in the vicinity of both a critical point of charge concentration and a deep ESP minimum. This analysis evidences the role of local factors (the charge concentrations around oxygen atoms) in determining the *position* of the ESP minima. The charge concentrations around the oxygen sites could also influence the *relative ordering* of those minima. As a matter of fact, the most important charge concentration around oxygen is found near O_B ($-\nabla^2\rho$ = 3.09 au), in probable relation with the convergent charge polarizations arising from the opposite metal tripod. The next higher maxima of $-\nabla^2\rho$ correspond to the twin charge concentrations around the D sites ($-\nabla^2\rho$ = 2.84 au, Table II), immediately followed by the concentrations in the nonbonding regions of O_C (2.83 au). The correlation with the values of the ESP minima is not straightforward, since a large potential gap does exist between the ESP minima around C and D, accounting for the nonlocal effects (Table II). However, the coincidence between (i) the lowest ESP minimum, (ii) the most important charge concentration, and (iii) the preferred site of protonation in $[HV_{10}O_{28}]^{-5}$ is certainly not fortuitous.[25] Let us finally stress that the topology of the electron distribution associated with the ionic VO bond is quite different from that of a M–L coordinative bond. The coordinative bond is characterized by a (3, +3) cp close to the metal, facing a maximum of charge concentration ((3, −3) cp) on the ligand side. Those critical points are easily interpretable in terms of the "empty metal orbital" facing the "ligand lone pair".[21]

The last section of this discussion will be devoted to the analysis of the distribution of $-\nabla^2\rho$ around vanadium atoms. At variance

(25) Bader et al. have proposed in previous studies[12,13] that regions of charge concentration and charge depletion as defined from the critical points of $-\nabla^2\rho$ should be used to identify the sites of electrophilic or nucleophilic attack.

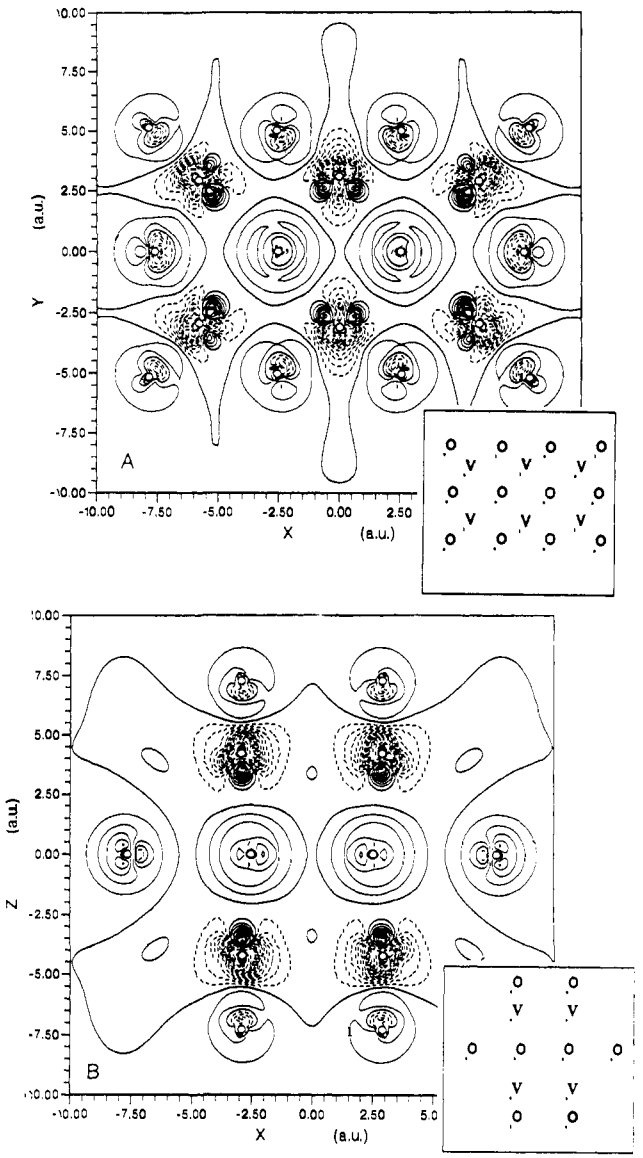

Figure 16. Electron deformation density with respect to a superposition of neutral atoms: (A, top) *xy* plane; (B, bottom) *xz* plane. Bold line, zero contour; solid lines, positive contours; dotted lines, negative contours; contour interval, 0.1 eÅ^{-3}.

from the near-spherical distribution found in the valence region of oxygen atoms, the metal i-VSCC is highly polarized. Six maxima in $-\nabla^2\rho$ are characterized around the V_1 and the V_2 atoms. Figure 15 displays the orientation of those maxima around V_2 in the *xy* plane. A hasty examination of Figure 15A could lead to the erroneous conclusion that the (3, −3) critical points approximately coincide with the directions of the four V–O bonds. In fact, the average deviation reaches 13.3° and a much better correlation (average deviation 4.1°) is obtained when the direction of the critical point is compared with that of the *opposite* V–O bond. Further analysis confirms this interpretation, which agrees with the ionic V–O bond being defined as a "closed-shell interaction" generating charge concentrations *away* from the interatomic surface.[17-19] Arguments are as follows:

(i) V_3 exhibits a significant pyramidalization of the equatorial V–O bonds (Figure 1). The (3, −3) critical points generate a square bipyramid, the basis of which is not coincident but opposite to that formed by the V_3–O_B and V_3–O_C bonds.[26]

(26) No (3, −3) critical point of charge concentration could be detected in the *axial* direction V_3–O_F, that is, opposite to V_3–O_A. A (3, −1) critical point only was characterized in that direction, in probable relation with the weakness of the V_3–O_A interaction and with the close vicinity of the four (3, −3) critical points opposite to the equatorial V–O bonds.

Table III. Maxima in $-\nabla^2\rho$ Detected Around the Vanadium Atoms[a]

bond	d_{V-O} (Å)	$-\nabla^2\rho$ (au)	ρ_{cp}
V_2–O_G	1.605	19.3	1.812
V_3–O_F	1.614	19.0	1.802
V_1–O_E	1.697	18.4	1.750
V_3–O_C	1.826	16.6	1.667
V_2–O_D	1.831	16.9	1.676
V_2–O_C	1.883	15.7	1.631
V_1–O_B	1.927	15.1	1.607
V_3–O_B	2.013	14.1	1.563
V_2–O_E	2.032	14.1	1.561
V_1–O_A	2.116	12.3	1.497
V_3–O_A	2.243	...[b]	...[b]
V_2–O_A	2.316	11.3	1.456

[a] The (3, −3) critical points in the Laplacian distribution of ρ are associated with the *opposite* V–O bond distance. [b] See ref 26.

Table IV. Correlation between the OVO′ Angles and the Product of the $\nabla^2\rho$ Values at the Critical Points cp and cp′ Opposite to O and O′ with Respect to V

OVO′	OVO′ (deg)	cpVcp′ (deg)	$\nabla^2\rho(r_{cp})$	$\nabla^2\rho(r_{cp'})$	cp*cp′
A1A	78.5	73.9	−12.3	−12.3	151.8
A1B	80.8	77.9	−12.3	−15.1	185.7
A1E	87.6	92.1	−12.3	−18.4	226.4
B1E	97.1	99.5	−15.1	−18.4	277.8
E1E	106.2	101.9	−18.4	−18.4	338.6
A2E	75.0	76.8	−11.0	−14.1	155.1
A2C	77.6	78.7	−11.0	−15.7	172.7
A2D	80.0	88.5	−11.0	−16.9	185.9
C2E	84.0	84.0	−15.7	−14.1	221.4
C2D	90.7	93.2	−15.7	−16.9	265.3
G2E	100.2	94.6	−19.3	−14.1	272.1
G2C	102.1	100.6	−19.3	−15.7	303.0
G2D	104.8	100.2	−19.3	−16.9	326.2
B3B	76.4	78.8	−14.1	−14.1	198.2
B3C	89.5	90.1	−14.1	−16.6	234.4
C3C	95.6	95.3	−16.6	−16.6	277.2
B3F	100.0	97.2	−14.1	−19.0	267.5
C3F	102.6	100.4	−16.6	−19.0	316.4

(ii) No correlation can be found between the *value* of $-\nabla^2\rho$ at the critical point and the *length* of the closest V–O bond. At variance from that, an inverse correlation clearly appears between $-\nabla^2\rho$ and the V–O bond length *opposite to the critical point*, as displayed in Table III.

(iii) The deformation density maps[27] obtained in two perpendicular planes both containing the two O_A oxygens together with different vanadium sites (Figure 16) display regions of density accumulation around all vanadium atoms. *Those accumulations are consistently oriented toward the O_A atoms.* Since the V–O_A distances are the longest V–O bonds in the cluster, the density accumulations can be interpreted as the counterpart of the charge depletion occurring along the opposite, and shorter, V–O bonds. In the case of nonbonded interactions, illustrated by the case of He_2, the density is shifted from the central region of the bond into the outer part of the nuclei.[28] Assimilating the ionic V–O bonds to closed-shell interactions, the density is *depleted in the inner part of the strongest bonds* and accumulated in the outer region, that is, *toward the weakly bonded O_A atoms.*

The above considerations clearly establish a linkage between the orientation of the charge concentrations around vanadium and that of the opposite V–O bonds. However, the question of which orientation determines the opposite one has not been answered

(27) The deformation density distribution is defined as

$$\Delta\rho = \rho_{mol} - \sum\rho_{atom}$$

where ρ_{mol} is the computed molecular density, and $\Sigma\rho_{atom}$ represents the density generated by a superposition of spherically averaged atoms computed in their ground state.

(28) Schwarz, W. H. E.; Valtazanos, P.; Ruedenberg, K. *Theor. Chim. Acta* **1985**, *68*, 471.

Table V. Atomic Point Charges (e) Deduced from the Standard and from a Modified Version of the Mulliken Population Analysis and Computed from Density Integration

	standard Mulliken	modified Mulliken[a]	density integration[b]	connected V atoms
V_1	+2.13	+2.13		
V_2	+2.04	+2.04		
V_3	+2.05	+2.05		
O_A	−2.62	−1.27	−1.51	6
O_B	−0.94	−1.04		3
O_C	−0.89	−0.93		2
O_D	−0.88	−0.94		2
O_E	−0.75	−0.82	−1.02	2
O_F	−0.68	−0.63	−0.85	1
O_G	−0.74	−0.66	−0.89	1

[a] The contribution of the most diffuse Gaussian function on oxygen has been discarded. [b] The net charge of oxygen sites has been computed by integrating the density over the domain defined by the surface of zero gradient flux

yet. In other words, could the value of the OVO angles be influenced by the electrostatic repulsion of the opposite charge concentrations? Figure 15B provides the hint of a positive answer. It shows, on the one hand, that the angle between two critical points around the vanadium atom, very close to the opposite OVO angle (cp–V–cp′ = 100.2°, OVO = 104.8°), is maximum between the two highest values of $-\nabla^2\rho$. On the other hand, the cp–V–cp′ angle is minimum (76.8°) as the opposite OVO angle (75.0°) between the two smallest charge concentrations. Table IV systematically extends this correlation by comparing the product of the values of $-\nabla^2\rho$ for all pairs of neighboring cp's with both the cp–V–cp′ angles and the opposite OVO angles. Although some values are going against the trend (for example, $O_AV_2O_D$ and $O_CV_2O_E$), it is clear that the cp–V–cp′ angle is increasing with the $(\nabla^2\rho(\text{cp})) \times (\nabla^2\rho(\text{cp}'))$ product. The correlation is still more remarkable when carried out with respect to the opposite OVO angles. In conclusion, one should notice that the geometry of the decavanadate cage could result from an electrostatic feedback process since the charge concentrations around vanadium increase with the strength, decrease with the elongation of the opposite V–O bond, and then contribute to govern the value of the opposite OVO angles.[29]

A final remark concerns the interpretation of the polarized i-VSCC of vanadium atoms. No sign of spd hybridization could be detected, the distribution of the 3p electrons remaining basically spherical. This first shows the inadequacy of the purely ionic model $V^{5+}O^{2-}$, which does not allow for any population of the 3d shell, and consequently for any charge concentration arising from that shell. Then, the exclusive polarization of the d electrons rules out for the present molecule the correspondence that had been proposed for AX_n systems between charge concentrations and electron pairs.[30] In a more general way, the extension to transition metal complexes of the correspondence proposed by Bader, Gillespie, and MacDougall is not obvious, because the ns and np shells should be considered as belonging to the core, and the associated electrons are not readily available for spd hybridization. Other cases have been recently discussed where the number of charge concentrations in the metal i-VSCC exceeds the number of valence electron pairs.[21]

5. Atomic Point Charges

It has been shown above that the validity of the purely ionic model $V^{5+}O^{2-}$ is questionable, since it does not account for the presence of 3d charge concentrations in the metal i-VSCC. The determination of atomic point charges is therefore of interest in order to provide an indication of how much the real bonding departs from the purely ionic description. The Mulliken charges are reported in Table V. Unfortunately, the poor quality of the Mulliken space partitioning is aggravated in the present case by the presence of diffuse basis functions on oxygen atoms. The obtained results are clearly artificial, as indicated, for example, by the net charge of −2.62 e attributed to the O_A atoms. A more consistent point charge distribution was obtained by discarding the contribution of the oxygen diffuse function (Table V). This contribution globally amounts to 2.14 e that is not attributed to any center. The population of the oxygen atoms is therefore underestimated. A more realistic space partitioning has been proposed by Bader et al. and consists in defining the atomic domain as the three-dimensional basin limited by the surfaces of zero-gradient flux.[31] Charge integration has been carried out on such domains for some oxygen sites (Table V). The obtained net charges are −1.51 e for O_A, −0.85 e and −0.89 e for the F and G terminal sites, and −1.02 e for the E bridging site. The negative net charge is consistently shifted by 0.20 to 0.23 e with respect to the modified Mulliken values, and a similar shift can be expected to yield reliable charges for the other sites.[32] Assuming this hypothesis, the negative net charge of an oxygen site consistently decreases with the number of vanadium atoms to which it is connected. The only oxygen atoms that can be reasonably described as O^{2-} are those located inside the double cage and connected each to six vanadium atoms. The deformation density maps of Figure 16 and the lack of (3, −3) cp for $\nabla^2\rho$ in the xy plane confirm the near-spherical symmetry of the charge distribution around O_A. All other, "external" oxygens, are expected to carry a charge that is either somewhat above or slightly below 1 e, and characterized by a more visible deviation from the spherical symmetry (Figure 16). Relying on the Mulliken analysis and on the effect of density integration on oxygen charges, the metal net charges should remain similar for the three vanadium sites, and reach ∼+2.4 e.

6. Conclusion

The topological analysis of the electrostatic potentials and the determination of the charge concentrations in the vicinity of the oxygen sites, both obtained from an ab initio SCF wave function of the decavanadate ion, provide convergent indications concerning the relative basicity of the six external oxygen sites. Several ESP minima have been characterized, most of them, but not all, lying in the vicinity of a specific oxygen atom. The deepest minimum is associated with site B, which has the greatest number of nearest neighbors on the planar closest packed oxygen surface. The second deepest minimum is located in the vicinity of site C. This ordering quite agrees with the interpretation of the ^{17}O NMR spectrum proposed by Klemperer and Shum.[3] The angular orientation of these minima with respect to the neighboring atoms is similar within a few degrees to that of the hydrogen atoms attached to one B site and two C sites in $[H_3V_{10}O_{28}]^{3-}$. The orientation of the ESP minima, when existing, also correlates with that of the charge concentrations characterized from the (3, −3) critical points of the Laplacian of ρ in the vicinity of the oxygen sites. The highest maximum in $-\nabla^2\rho$ and the deepest ESP minimum are both associated with site B, indicating that local effects could act in synergy with the steric crowding on the oxygen surface to favor the centrally located oxygen (O_B) as the most attractive site for protons or small cationic groups. Important concentrations of charge, arising in the 3d shell, are found in the vicinity of the vanadium atoms, in directions opposite to the V–O bonds. The repulsion between pairs of charge concentrations probably contributes to determine the opposite OVO angle. Finally, atomic point charges significantly depart, except for the internal O_A sites, from the purely ionic bonding model $V^{5+}O^{2-}$. The negative charge on oxygen consistently increases with the number of connected metal atoms. The net charge on the three vanadium sites is estimated to ∼+2.4 e.

(29) One could also argue that the correlation between cpVcp′ and $(\nabla^2\rho(\text{cp})) \times (\nabla^2\rho(\text{cp}'))$ just reflects the trend of two short V–O bonds to repel each other.

(30) Bader, R. F. W.; Gillespie, R. J.; MacDougall, P. J. *J. Am. Chem. Soc.* **1988**, *110*, 7329.

(31) Bader, R. F. W.; Nguyen-Dang, T. T. *Adv. Quantum Chem.* **1981**, *14*, 63.

(32) Technical problems were encountered for defining the integration domain of the Lagrangian distribution associated with oxygen sites B, C, and D.

Acknowledgment. The calculation of the SCF wave function has been carried out on the Cray-2 computer of the Ecole Polytechnique Fédérale de Lausanne (Switzerland). We are very much indebted to Professor P.-A. Carrupt for introducing us to the CC of the EPFL, and to Dr. A. Possoz, for her constant help throughout this project. We are also pleased to thank Dr. R. Ernenwein (Cray-Research France) for high-level computational assistance. The ESP have been derived on the Cray-2 computer of the Centre de Calcul Vectoriel de la Recherche (Palaiseau, France) through a grant of computer time from the Conseil Scientifique du CCVR. The investigations on the distribution of $\rho(r)$ have been carried out with the IBM 3090 of the Centre d'Informatica de la Universitat de Barcelona (Spain) and with an IBM RISC 6000 purchased with funds provided by the CYCIT (PB89-0648-C02-02). We are very much indebted to Professor R. F. W. Bader for a copy of the AIMPAC package of programs.

Mechanism of the Ziegler Dilithiomethane Synthesis. An ab Initio Study of Methyllithium Pyrolysis

Nicolaas J. R. van Eikema Hommes,[†] Paul von Ragué Schleyer,*[,†] and Yun-Dong Wu[‡]

Contribution from the Institut für Organische Chemie der Friedrich-Alexander-Universität Erlangen-Nürnberg, D-8520 Erlangen, Federal Republic of Germany, and Department of Chemistry and Biochemistry, University of California, Los Angeles, Los Angeles, California 90024. *Received July 19, 1991*

Abstract: Ziegler's disproportionation reaction of methyllithium to give dilithiomethane and methane upon heating to 225 °C is predicted by ab initio theory (MP2/6-31+G*//6-31G*) to proceed endothermically through a polar hydrogen-transfer mechanism within a tetrameric methyllithium aggregate, $(CH_3Li)_4 \rightarrow CH_2Li_2 \cdot (Li/CH_3)_2 + CH_4$. A free energy of reaction of +19.6 kcal/mol and an activation barrier ($\Delta G^{\ddagger}$) of 53.8 kcal/mol at 500 K are computed. The alternative reactions within dimeric and trimeric aggregates are endothermic by 31.1 and 21.4 kcal/mol at MP4SDTQ/6-31+G*//6-31G* with activation barriers of 64.3 and 58.2 kcal/mol, respectively. Under the reaction conditions, methyllithium trimers should be in equilibrium with tetramers, but tetramers are still expected to be the predominant species.

Introduction

In 1955, Ziegler, Nagel, and Patheiger reported the preparation of dilithiomethane by pyrolysis of methyllithium (eq 1).[1] The product, a highly pyrophoric insoluble powder, showed erratic behavior: Its reactions were reported to proceed explosively or, in other experiments, very sluggishly with the same reagent under the same conditions.[2] Apart from a few IR signals,[3] no information concerning the molecular structure was available until the first computational studies by Schleyer and Pople et al.[4] 20 years later. They discovered that dilithiomethane, as well as some other geminal dilithio compounds, have a remarkably small energy difference between the planar and the usual "tetrahedral" geometries. The same was found to be true for the dilithiomethane triplets, which have nearly the same energies as the singlets. These results not only stimulated much theoretical work[5] but also revived the experimental interest in this class of compounds.[6-9] Lagow and his group optimized the Ziegler pyrolysis[6] and developed it into a general method for the preparation of a large variety of geminal dilithiated compounds (Chart I).[7] The dilithiated products are obtained in moderate to good yields and can be useful intermediates in the synthesis of other organometallic compounds.[8d]

$$2nH_3CLi \rightarrow (H_2CLi_2)_n + nCH_4 \qquad (1)$$

Detailed investigations of dilithiomethane and its dideuterio derivative[6,10] culminated recently in the successful determination of the powder neutron diffraction structure of dideuteriodilithiomethane.[11] The structure proved to be much more complex than that anticipated by model ab initio calculations on small aggregates:[5b] In the three-dimensional polymeric network, each methylene "dianion" is surrounded by no fewer than *eight* lithium cations!

The mechanism of the Ziegler disproportionation reaction is unknown. Prolonged heating and careful removal of the gaseous products are required.[6] This suggests that the reaction is endothermic and is driven by the loss of the volatile byproducts.

Chart I

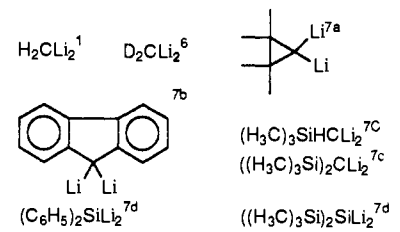

Furthermore, the use of halide-free monolithium compounds is essential,[8b] e.g., the use of commercial methyllithium, which

[†] Friedrich-Alexander-Universität Erlangen-Nürnberg.
[‡] University of California, Los Angeles.

(1) Ziegler, K.; Nagel, K.; Patheiger, M. *Z. Anorg. Allg. Chem.* **1955**, *282*, 345.
(2) Krohmer, P.; Goubeau, J. *Chem. Ber.* **1971**, *104*, 1347.
(3) Krohmer, P.; Goubeau, J. *Z. Anorg. Allg. Chem.* **1969**, *369*, 238.
(4) Collins, J. B.; Dill, J. D.; Jemmis, E. D.; Apeloig, Y.; Schleyer, P. v. R.; Seeger, R.; Pople, J. A. *J. Am. Chem. Soc.* **1976**, *98*, 5419.
(5) (a) Laidig, W. D.; Schaefer, H. F., III. *J. Am. Chem. Soc.* **1978**, *100*, 5972. (b) Jemmis, E. D.; Schleyer, P. v. R. *J. Organomet. Chem.* **1978**, *154*, 327. (c) Bachrach, S. M.; Streitwieser, A., Jr. *J. Am. Chem. Soc.* **1984**, *106*, 5818. (d) Alvarado-Swaisgood, A. E.; Harrison, J. F. *J. Phys. Chem.* **1985**, *89*, 62. (e) Ritchie, J. P.; Bachrach, S. M. *J. Am. Chem. Soc.* **1987**, *109*, 5909.
(6) Gurak, J. A.; Chinn, J. W., Jr.; Lagow, R. J.; Steinfink, H.; Yannoni, C. *Inorg. Chem.* **1984**, *23*, 3717.
(7) (a) Kawa, H.; Manley, B. C.; Lagow, R. J. *J. Am. Chem. Soc.* **1985**, *107*, 5315. (b) Chauhan, H. P. S.; Kawa, H.; Lagow, R. J. *J. Org. Chem.* **1986**, *51*, 1633. (c) Kawa, H.; Manley, B. C.; Lagow, R. J. *Polyhedron* **1988**, *7*, 2023. (d) Mehrotra, S. K.; Kawa, H.; Ludvig, M. M.; Lagow, R. J. *J. Am. Chem. Soc.* **1990**, *112*, 9003.
(8) (a) Maerker, A.; Theis, M.; Kos, A. J.; Schleyer, P. v. R. *Angew. Chem.* **1983**, *95*, 755; *Angew. Chem., Int. Ed. Engl.* **1983**, *22*, 733. (b) Maerker, A.; Dujardin, R. *Angew. Chem.* **1984**, *96*, 222; *Angew. Chem., Int. Ed. Engl.* **1984**, *23*, 224. (c) Kawa, H.; Chinn, J. W., Jr.; Lagow, R. J. *J. Chem. Soc., Chem. Commun.* **1984**, 1664. (d) Vollhardt, J.; Gais, H.-J.; Lukas, K. L. *Angew. Chem.* **1985**, *97*, 695; *Angew. Chem., Int. Ed. Engl.* **1985**, *24*, 610. (e) Pilz, M.; Allwohn, J.; Hunold, R.; Massa, W.; Berndt, A. *Angew. Chem.* **1988**, *100*, 1421; *Angew. Chem., Int. Ed. Engl.* **1988**, *27*, 1370. (f) van Eikema Hommes, N. J. R.; Bickelhaupt, F.; Klumpp, G. W. *Tetrahedron Lett.* **1988**, *29*, 5237. (g) Gais, H.-J.; Vollhardt, J.; Günther, H.; Moskau, D.; Lindner, H. J.; Braun, S. *J. Am. Chem. Soc.* **1988**, *110*, 978. (h) Zarges, W.; Marsch, M.; Harms, K.; Boche, G. *Chem. Ber.* **1989**, *122*, 1307. (i) Baran, J. R., Jr.; Lagow, R. J. *J. Am. Chem. Soc.* **1990**, *112*, 9415. (j) van Eikema Hommes, N. J. R.; Bickelhaupt, F.; Klumpp, G. W. *J. Chem. Soc., Chem. Commun.*, **1991**, 438.

0002-7863/92/1514-1146$03.00/0